ELSEVIER

Contents lists available at ScienceDirect

# **Materials Characterization**

journal homepage: www.elsevier.com/locate/matchar



# Application of chord length distributions and principal component analysis for quantification and representation of diverse polycrystalline microstructures



Marat I. Latypov<sup>a,b,\*</sup>, Markus Kühbach<sup>c</sup>, Irene J. Beyerlein<sup>a,b</sup>, Jean-Charles Stinville<sup>b</sup>, Laszlo S. Toth<sup>d</sup>, Tresa M. Pollock<sup>b</sup>, Surya R. Kalidindi<sup>e,f</sup>

- <sup>a</sup> Mechanical Engineering Department, University of California, Santa Barbara, CA 93106, USA
- <sup>b</sup> Materials Department, University of California, Santa Barbara, CA 93106, USA
- <sup>c</sup> Max-Planck-Institut für Eisenforschung GmbH, Max-Planck-Straße 1, D-40237 Düsseldorf, Germany
- d University of Lorraine, Laboratory of Excellence on Design of Alloy Metals for Low-mAss Structures (DAMAS), Metz 57073, France
- <sup>e</sup> Woodruff School of Mechanical Engineering, Georgia Institute of Technology, Atlanta, GA 30332, USA
- f School of Computational Science and Engineering, Georgia Institute of Technology, Atlanta, GA 30332, USA

#### ARTICLE INFO

# Keywords: Microstructure Chord length distribution Grain size Principal component analysis

#### ABSTRACT

Quantification of mesoscale microstructures of polycrystalline materials is important for a range of practical tasks of materials design and development. The current protocols of quantifying grain size and morphology often rely on microstructure metrics (e.g., mean grain diameter) that overlook important details of the mesostructure. In this work, we present a quantification framework based on directionally resolved chord length distribution and principal component analysis as a means of extracting additional information from 2-D microstructural maps. Towards this end, we first present in detail a method for calculating chord length distribution based on boundary segments available in modern digital datasets (e.g., from microscopy post-processing) and their low-rank representations by principal component analysis. The utility of the proposed framework for capturing grain size, morphology, and their anisotropy for efficient visualization, representation, and specification of polycrystalline microstructures is then demonstrated in case studies on datasets from synthetic generation, experiments (on Ni-base superalloys), and simulations (on steel during recrystallization).

# 1. Introduction

Material structure, i.e., *microstructure*, plays an essential role in guiding all materials innovation efforts aimed at improving the property combinations [1,2]. One of the central challenges in the field comes from the lack of rigorous approaches for the quantification of the microstructure. Our focus in this work is on the microstructures encountered in metallic samples, where the shape and size distributions of the individual grains (i.e., volumes of uniform crystal lattice orientation) dominate the microstructural considerations. These polycrystalline microstructures are typically studied at length scales in the range of 0.1 to  $100\,\mu m$ , where the grains are separated by grain boundaries. The grain structure in polycrystalline materials is naturally associated with a number of potential measures of the microstructure that can be used in the effort to capture its salient features. These measures include

distributions of sizes, shapes, and orientations of grains and their interfaces [3–5]. In this work, we focus our attention on the rigorous quantification of the grain size and morphology characteristics because of their anticipated strong impact on a range of mechanical and physical properties [6–14]. One such well-known effect is in the dependence of the effective yield strength of the material on the average grain size (e.g., Hall–Petch laws [6,7]). While there is general agreement on the importance of the grain size in controlling the properties of the material, the exact definitions, measures, and characterization techniques used in the quantification of the grain size vary significantly among the practitioners. For example, given a microstructure image, protocols employed in practice include estimations of the grain size based on either intercept lengths or grain areas/volumes or grain boundary lengths/areas, which contributes to inconsistencies in the reports of the average grain size.

<sup>\*</sup> Corresponding author at: Mechanical Engineering Department, University of California, Santa Barbara, CA 93106, USA. E-mail addresses: latmarat@ucsb.edu (M.I. Latypov), m.kuehbach@mpie.de (M. Kühbach), beyerlein@ucsb.edu (I.J. Beyerlein), stinville@engineering.ucsb.edu (J.-C. Stinville), laszlo.toth@univ-lorraine.fr (L.S. Toth), pollock@engineering.ucsb.edu (T.M. Pollock), surya.kalidindi@me.gatech.edu (S.R. Kalidindi).

Area-based estimations of the grain size are becoming the methods of choice in modern characterization efforts that yield digital pixelated datasets (e.g., digital optical micrographs, back-scattered electron images from scanning electron microscope, electron back-scattered diffraction maps). Grain areas can be readily extracted from such datasets by simply counting the number of pixels contained in each grain. Once the grain area is known, it is common practice to estimate the grain size as the diameter of an equivalent circle (henceforth referred to as the grain diameter) of the same area as the grain. The use of the grain diameter thus implicitly assumes that the grain shape is close to a circle. Similar approaches are being adopted for 3-D datasets, in which grain diameter can be obtained from the average grain volume and the consideration of an equivalent sphere [15,16]. The diameters of individual grains are typically averaged to provide for a scalar measure of the grain size of the material. As an extension of this approach, grain diameters are also often reported as distributions (i.e., histograms) that quantify the number fraction or the area fraction for each discretized bin of grain diameters [17]. Alternatively, some authors have fit the sampled grain diameters to log-normal distributions [18,19,11,12].

Despite its utility and wide adoption, the use of grain diameter leads to a loss of information regarding the distributions of grain shape and its alignment. Within the area-based approaches, some efforts have accounted for the grain shape by fitting the grain areas to equivalent ellipsoids (instead of circles/spheres) [20,3], and obtaining distributions of the major axis length, the minor axis length, and their inclination angles (e.g., [21]). The fundamental limitation of these approaches is that the grains in many samples do not really fit any specific idealized shape. This is particularly the case in microstructures of solidified [22], welded [11,12], or additively manufactured metals [16].

The approaches of estimating the grain size based on intercepts (or chords) have the potential to overcome the limitations of the area-based approaches described above. Grain size estimations based on chord lengths have a long history going back to early methods for metallographic observations [23]. Furthermore, chord length distribution (CLD), which describes the probability of finding chords of a specified length in the microstructure [24], is expected to be highly relevant to properties related to free paths in heterogeneous materials (e.g., plastic properties [4,8,9], transport properties [24,25]). Chords are defined as line segments traversing the entire grain, which originate on one grain boundary and end on the next grain boundary encountered. Chords are typically sampled by placing test lines on the microstructure, and either measuring distances between intersections of the test lines and grain boundaries or counting the number of such intersections [26]. In most reported studies, chord lengths were sampled either in randomly selected directions [26-28] or in a few specifically selected directions (e.g., along principal axes of the microstructure image [29,11,12]). For example, Lehto et al. [11,12] developed an image processing algorithm to obtain chord lengths in four directions of the microstructure (0°, 45°, 90°, and 135°, with subsequent averaging according to the standard [27]) to obtain the average grain size as well as its spatial variations in highly heterogeneous samples of welded steel.

A limited number of prior studies [8,9,30] have targeted chord lengths in directions beyond the principal axes. Fromm et al. [8] introduced a grain size and orientation distribution function (GSODF) that was evaluated using chord lengths in specific directions in each grain related to its slip systems. The grain size estimated in this manner was incorporated into a Taylor-type polycrystal plasticity model of h.c.p.  $\alpha$ -Ti to study the effects of crystallographic texture and grain size distribution on the macroscopic mechanical response of the material. Sun and Sundararaghavan [9] extended the above concept by accounting individually for the available slip lengths for each slip system in a selected grain and modeled its evolution during the imposed large plastic strains on the sample. Turner et al. [30] presented a scan-line approach to computationally efficient calculations of CLDs for the full range of directions in 2-D and 3-D microstructures, and demonstrated their approaches on a number of composite microstructures. Their

algorithm scans over all pixels of digital microstructure images and simply counts the number of voxels inside every microstructure constituent along the scan line. While such pixel-based computations are straightforward along the principal axes of microstructure images, other directions require special treatment such as the use of Bresenham lines [31].

In this contribution, we approach the quantification of the grain structure in metallic samples using angularly resolved CLD and its lowrank representation using principal component analysis (PCA). In this effort, we will develop and utilize an approach that takes advantage of the grain boundary segments that can be identified and extracted from modern characterization techniques such as electron back-scattered diffraction (EBSD) [3]. This method of CLD calculations offers an alternative to the scan-line approach [30] mentioned earlier that identifies boundaries only indirectly by the changes in phase content (or grain orientation) between neighboring pixels. A potential advantage of explicitly representing the grain (or phase) boundary segments with continuous coordinates is that it lends itself to easier conversion to a conformal finite element mesh [32] for the analyses of mechanical response. The second contribution of this work is in the extraction of the low-dimensional representations that are likely to be highly valuable in at least two aspects: (i) classification and visualization of large and diverse ensembles of microstructures, and (ii) the formulation of datadriven process-structure-property linkages [33-36]. In this work, we will focus mainly on the viability of using PCA as an effective dimensionality-reduction strategy in the classification of a diverse set of grain morphologies in polycrystalline microstructures.

# 2. Angularly Resolved Chord Length Distribution

# 2.1. New Boundary-based Approach for CLDs

In the present study, we develop and employ an approach based on geometrical considerations of boundary segments in the microstructures being studied. Boundary segments, defined as straight segments between two adjacent points along a grain boundary, can be extracted from routine post-processing of datasets obtained from both experiments (e.g., grain boundaries established by thresholding misorientations in EBSD maps) and simulations (e.g., grain boundary contours tracked by recrystallization simulations [37]). At the core of the approach presented here is the computation of coordinates of intersection points between test lines and boundary segments.

We start by considering two arbitrary line segments, AB and CD, in 2-D space with end points  $\mathbf{A}(x_A, y_A)$ ,  $\mathbf{B}(x_B, y_B)$ ,  $\mathbf{C}(x_C, y_C)$ , and  $\mathbf{D}(x_D, y_D)$ , respectively. The parametric equations describing all the points on these line segments can be expressed as [38]:

$$\mathbf{P}_{AB} = \mathbf{A} + t_{AB}(\mathbf{B} - \mathbf{A}),\tag{1a}$$

$$\mathbf{P}_{CD} = \mathbf{C} + t_{CD}(\mathbf{D} - \mathbf{C}),\tag{1b}$$

with  $t_{AB} \in (0,1)$  and  $t_{CD} \in (0,1)$ .

The coordinates of the intersection point between the two segments can be found by setting  $\mathbf{P}_{AB} = \mathbf{P}_{CD}$ , which yields a system of two linear equations (corresponding to two coordinates in two dimensions) with two unknowns,  $t_{AB}$  and  $t_{CD}$ . Bourke [39] provided solution for the problem as follows:

$$t_{AB} = \frac{(x_D - x_C)(y_A - y_C) - (y_D - y_C)(x_A - x_C)}{(y_D - y_C)(x_B - x_A) - (x_D - x_C)(y_B - y_A)},$$
(2a)

$$t_{CD} = \frac{(x_B - x_A)(y_A - y_C) - (y_B - y_A)(x_A - x_C)}{(y_D - y_C)(x_B - x_A) - (x_D - x_C)(y_B - y_A)},$$
(2b)

which gives the coordinates of the intersection point,  $T(x_T, y_T)$ , as

$$x_T = x_A + t_{AB}(x_B - x_A),$$
 (3a)

$$y_T = y_A + t_{AB}(y_B - y_A).$$
 (3b)

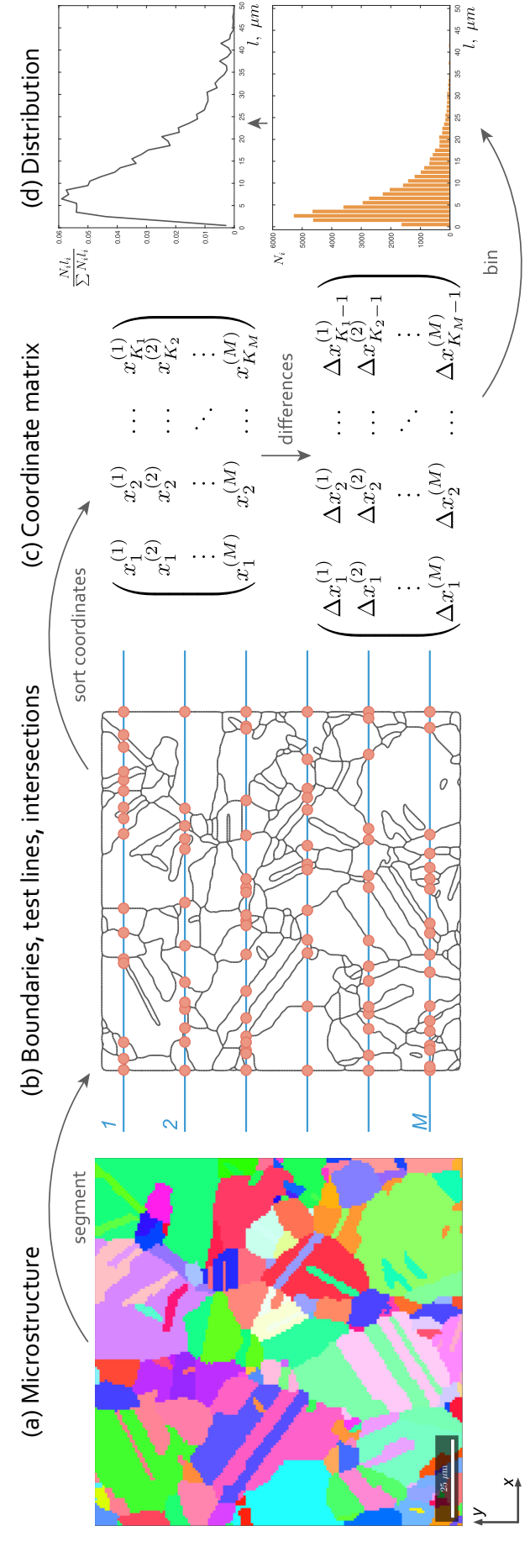


Fig. 1. Illustration of the present boundary based approach for obtaining chord length distributions: (a) synthetically generated example microstructure with elongated grains, (b) boundary map with superimposed test lines as well as intersections between them, (c) sorted coordinate matrix and its row-wise differences, (d) chord length distribution by binning chord length values.

The intersection point  $T(x_T, y_T)$  exists within the two segments if  $t_{AB}$  and  $t_{CD}$  both have values in the range between 0 and 1 [39].

The advantage of the geometric considerations described above is that they allow matrix-based computations. In the present context, it entails determination of intersection points for a number of test lines and boundary segments without looping through individual boundary segments or test lines. The intersection points so obtained can be further used for calculations of chord lengths, also in a matrix-based form. Consider, for example, a grain boundary map consisting of numerous grain boundary segments and a set of *M* parallel test lines placed on the boundary map parallel to the x axis (see Fig. 1a-b). Eqs. (3) can be implemented such that coordinates of the intersection points are stored into matrices with M rows (enumerated by m for each test line) and K columns (enumerated by k). In our example with horizontal test lines, the y coordinates of intersection points along each test line are constant and known as equal to the y coordinate of the test line. Consequently, only the matrix of the x coordinates, denoted by X, needs to be computed and stored. Furthermore, chord lengths along each test line are simply equal to differences in the x coordinates of neighboring intersection points (stored as the  $\Delta X$  matrix). Therefore, chord lengths can be obtained by two operations on the X matrix: row-wise sorting of elements and subsequent calculation of pairwise differences of the neighboring elements (Fig. 1c).

These matrix-based computations that avoid loops through boundary segments and test lines are efficient for relatively small microstructure maps. However, since such approach relies essentially on construction of an "interaction" matrix between all boundary segments and all test lines, these computations may become prohibitively memory-intensive for maps with a large number of boundary segments. For these situations, the algorithm can be modified to sequential computations of intersection points by considering one test line at a time. This alternative approach results in the identical procedure with the only difference that the X and  $\Delta X$  matrices shown in Fig. 1c consist of a single row each corresponding to a single test line per loop. When identifying intersection points between boundary segments and a single test line, computations can be further accelerated by considering only boundary segments that do intersect the current test line rather than the whole boundary map. These boundary segments can be found from the condition that the y coordinate of the test line lies between the y coordinates of the end points of the boundary segments.

Once the intersection points and consequently chord lengths are identified employing either matrix-based or sequential approach, binning chord length values provides for their distribution (Fig. 1d). From the binned chord length counts, CLD, as a step probability function, can be estimated as follows (no implicit summation on repeated index):

$$P_{l} = \frac{N_{i}l_{i}}{\sum_{i=1}^{n} N_{i}l_{i}},\tag{4}$$

where i enumerates chord length bins (from 1 to n),  $N_i$  is the number of chords sampled in the interval of the  $i^{\rm th}$  chord-length bin, whose center corresponds to the chord length  $l_i$ .  $P_l$  reflects the probability of finding a voxel that belongs to a chord of length l (within the range  $\Delta l$  used in the binning of the chord lengths). The CLD function defined in Eq. (4) implicitly satisfies the condition of  $\Sigma P_l = 1$ .

We also note that in all CLD analysis that follows, we will exclude intersection points between the test lines and the outer edges of a microstructure map from the calculations. Such line segments do not satisfy the definition of the chord (as a segment traversing the entire grain). It should be recognized that such exclusion makes for a much more efficient use of the limited information in a microstructural map compared to a complete removal of grains touching the edges (which is often done in practice). The exclusion of these line segments can be implemented by omission of the first and the last elements in each row of the  $\Delta X$  matrix. The only situation that we envision when such exclusion is not recommended is periodic microstructures (not considered

in this work); in this case, the edge line segments on the opposite sides along each test line should be summed to construct a single chord.

# 2.2. Angularly Resolved CLDs

The procedure described above for the calculation of chord length distribution for a grain structure in the x direction can be readily extended to an arbitrary direction. As discussed by Turner et al. [30], CLD can be calculated along directions other than the principal axes by either rotating the microstructure (or its image) or defining testing lines in the given direction. While image-based CLD calculations considered by Turner et al. require special image processing algorithms in the first case and special Bresenham lines in the second case, our method based on line segments allows both approaches within the same framework utilizing linear transformation of a set of line segments. In this work, we adopted the workflow with rotation of the boundary segments (i.e., microstructure) because our tests showed that this approach is more computationally efficient than rotation of the test lines. Since the grain boundary segments are defined by coordinates of their end points, the set of grain boundary segments can be rotated with the aid of a transformation matrix, Q:

$$\mathbf{b}' = \mathbf{Q}\mathbf{b},\tag{5}$$

where **b** denotes the set of coordinates of end points of grain boundary segments, and **b**' is the same set after transformation defined by matrix, **Q**. For our purposes, the transformation of interest is the active in-plane rotation about the axis normal to the plane containing the boundaries. Transformation matrix for active counter-clockwise rotation by an angle  $\theta$  in xy plane about the z axis is defined as:

$$\mathbf{Q} = \begin{pmatrix} \cos\theta & -\sin\theta \\ \sin\theta & \cos\theta \end{pmatrix} \tag{6}$$

For sampling chord lengths in the microstructure at an angle  $\theta$  (counter-clockwise from the x axis), one needs to rotate the boundary segments clockwise using  $-\theta$  in Eq. (6). Fig. 2a–b is a demonstration of finding intersection points between test lines and boundary segments rotated (clockwise) using Eqs. (5) and (6) to a few  $-\theta$  angles shown together with the corresponding CLDs computed in these directions as described in Section 2.1.

With the aid of rotation of grain boundary segments defined in Eqs. (5) and (6), angularly resolved CLDs (AR-CLDs) can be computed for the entire range of directions in 2-D, i.e., for  $\theta \in [0^{\circ}, 180^{\circ})$ . The selected range takes advantage of the two-fold symmetry of lines in 2-D, i.e., CLDs in directions defined by  $\theta$  and  $\theta + \pi$  are identical. Fig. 2c presents an example of an AR-CLD obtained for a synthetic microstructure by sampling directions in  $[0^{\circ}, 180^{\circ})$  with a 1° step and with test lines placed, for each direction, at a spacing equal to the grid step (see further details in Section 4.1).

The approach presented here is quite different from the scan-line method of Turner et al. [30] in that we do not use a voxelized description of the microstructural image. Instead, we only utilize continuous coordinates of the end points of the boundary segments. As a result, the present approach (i) does not require the representation and storage of the microstructure data on a regular grid, (ii) eliminates the need to loop over each pixel of the microstructure (which offers potential computational benefits for high-resolution data), and (iii) works naturally in any direction without special considerations such as Bresenham lines.

We finally note that the present approach to obtaining AR-CLDs can be parallelized owing to the independence of CLD calculations in different directions in the microstructure. This independence allows for

<sup>&</sup>lt;sup>1</sup> Active rotation is rotation of the object (in this case boundary segments) in respect to a fixed coordinate system, as opposed to passive rotation of the coordinate system in respect to a fixed object [40].

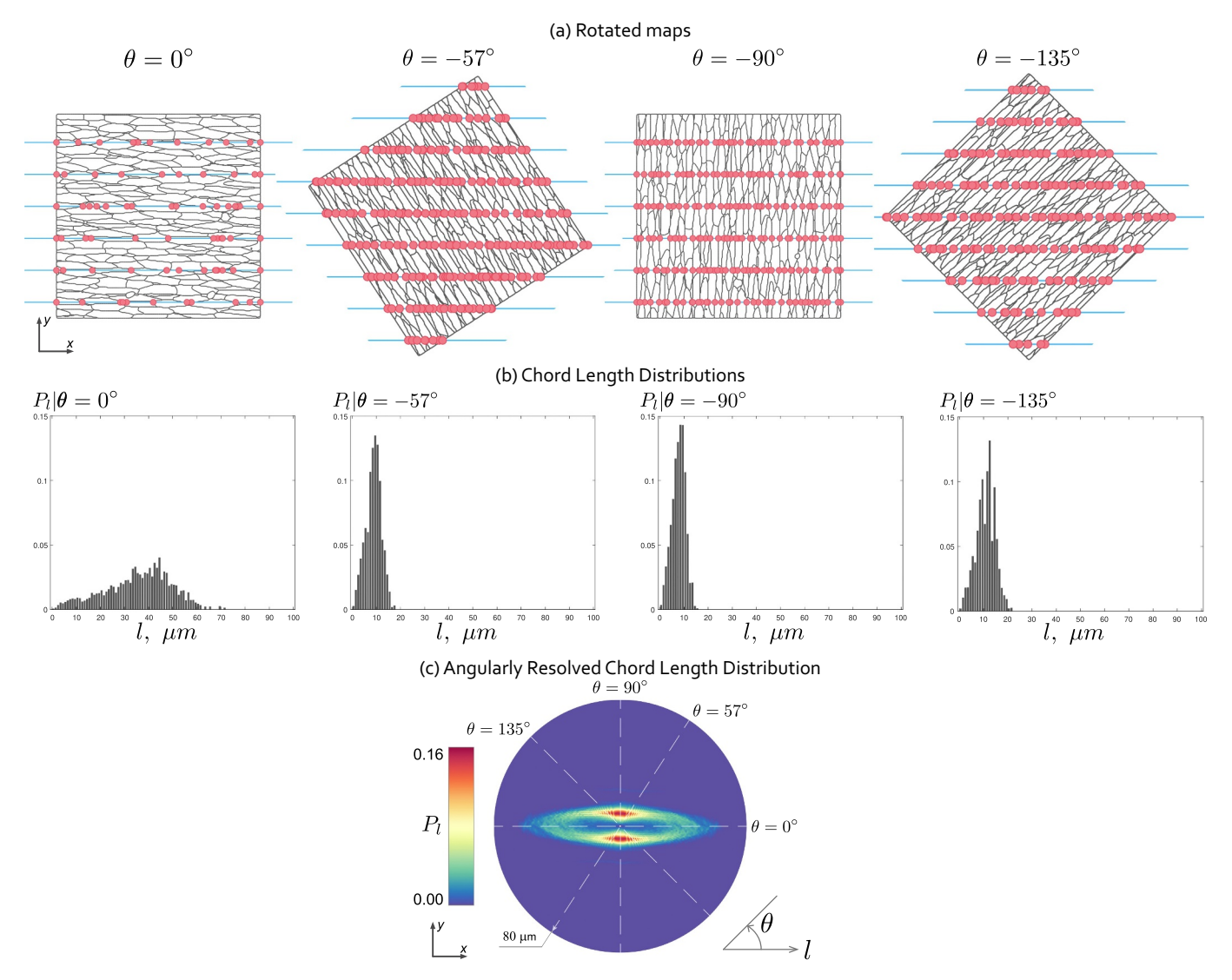


Fig. 2. Illustration of obtaining chord length distributions in different directions by clockwise rotations of boundary segments: (a) examples of rotated boundary segment maps to different angles  $\theta$ , (b) chord length distributions obtained along these directions, (c) angularly resolved chord length distribution calculated by sampling all directions in the range  $\theta \in [0,180^{\circ})$  with a 1° step. Note that only few test lines are shown in (a) for illustration purposes, whereas many more test lines are used throughout this paper (e.g., with spacing equal to the grid step for EBSD maps).

distribution of calculations in different directions among different CPUs (i.e., "trivial" parallelization).

To verify our algorithm, we compared results of CLD calculation as presented here to those obtained with the commercial software EDAX/TSL OIM [41], widely used by the materials characterization community. Verification test was carried out on an EBSD map experimentally measured in a Ni-base superalloy IN100 shown in Fig. 3a (see more details in Section 4.2). The CLDs are shown in two directions: along x and y axes because OIM software allows CLD calculations only along the principal axes. The CLDs using the present approach are obtained as described in Section 2.1 with 0° rotation for CLD along x axis and  $-90^{\circ}$  rotation of grain boundary segments (using Eq. (5)) for CLD along y axis. The comparison (Fig. 3b) shows excellent agreement between the results, verifying the algorithm presented in this work. Since the present algorithm is independent of the rotation angle, the agreement shown in Fig. 3 attests to the reliability of our method for CLDs computed in any direction.

# 2.3. Summary of the Workflow

The workflow for the boundary-based approach presented in this

work for obtaining AR-CLDs can be summarized as follows:

- 1. Identify boundary segments for the microstructure constituents of interest as an array of coordinates of the segment end points.
- 2. Define a set of test lines (parallel to one of the principal axes, e.g., *x* axis) as an array of coordinates of their end points. Ensure that the test lines cover the microstructure map and have a sufficiently small spacing compared to the characteristic size of the constituents (e.g., equal to grid step for voxelized maps).
- 3. Obtain intersection points between the test lines and the boundary segments using either matrix-based (small maps) or sequential (large maps) algorithms making use of Eqs. (2) and (3) and calculate chord lengths as pair-wise differences of sorted elements of the coordinate matrix. Estimate a distribution by binning chord length values and estimate the CLD as a step probability function (Eq. (4)).
- Repeat Step 3 for multiple directions in the microstructure by rotating the boundary segments to θ∈ [0, 180) with a small angular step (e.g., 1°) to obtain the AR-CLD.
- 5. Visualize the AR-CLD as a polar map, where the radial coordinate corresponds to the chord length, l, the azimuthal coordinate represents the direction in which CLD is probed (i.e.,  $\theta$  angle), and the

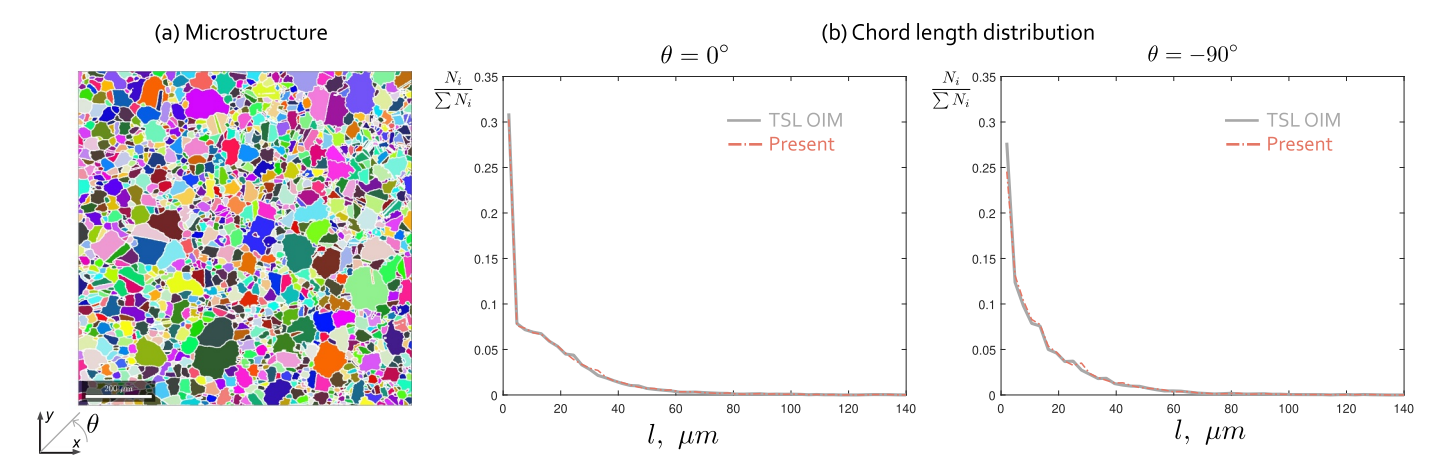


Fig. 3. Verification of the present approach to CLD calculation by comparison with results obtained using commercial software EDAX/TSL OIM: (a) test microstructure of IN100, (b) CLDs obtained along x and y axes.

color expresses the CLD,  $P_l(\theta)$ .

# 3. Principal Component Analysis

One of the main appeals of metrics such as the mean grain diameter is that they provide simple representations of complex microstructures by a single scalar quantity, which allows for convenient microstructure specification, comparison of effects of different sets of processing conditions on the microstructure as well as for incorporation of the microstructure into property prediction models. Richer statistical descriptions, such as the AR-CLD, on the other hand, come at the cost of significantly higher dimensionality. For example, the AR-CLD calculated for a synthetic microstructure in Fig. 2c contains 14,320 unique features (probability values for 80 chord length bins for each of the 179 sampled directions). While AR-CLDs provide for visually intuitive representations of microstructures, their relative quantitative comparisons or direct incorporation into practically useful models is challenging.

For overcoming the dimensionality burden for these purposes, data reduction techniques, such as principal component analysis (PCA) may be employed [42]. PCA is a linear, distance-preserving, transformation of data to a new orthogonal basis [42,43] that optimizes the capture of the variance in the data in the minimum number of terms (corresponding to the new PC basis). As a result, the number of variables in the new basis (i.e., principal component scores) required to represent the data with sufficient details is often dramatically smaller than the number of the original variables. This feature along with the property of preserving distances (which allows quantitative relative comparisons of the data points), renders PCA an extremely useful dimensionality reduction method for efficient visualization, noise reduction, and model development [42].

In the context of microstructure quantification, PCA can be used for reducing the dimensionality of statistical descriptions, and specifically AR-CLDs of ensembles of microstructures. In this case, PCA can be thought of as identification of patterns (basis vectors) in AR-CLDs and weights of these patterns (PC scores) that efficiently capture the variance in the statistical description of the microstructure ensemble. Once these patterns and their scores are identified, AR-CLD of any  $k^{\rm th}$  microstructure in the ensemble (or a new microstructure to be added to the ensemble) can be represented by their linear combination [44,45]:

$$P_l^{(k)} = \sum_{j=1}^J \alpha_j^{(k)} \phi_{jt} + \langle P_l \rangle, \tag{7}$$

where  $a_j^{(k)}$  are the PC scores,  $\phi_{jt}$  are basis vectors, obtained by PCA, and  $\langle P_l \rangle$  is the ensemble average AR-CLD. The dimensionality reduction

effect is achieved by truncating the series in Eq. (7) to the first R principal components such that  $R \ll J$ , which capture a desired level of variance in the ensemble and thus satisfies the equality condition in Eq. (7) to an approximation with well-defined accuracy. PCA applied on statistical description of microstructures has already proved useful for establishing quantitative processing–structure–property relationships in heterogeneous metallic materials [34,35,36,33].

#### 4. Case Studies

#### 4.1. Synthetic Datasets

The viability and advantages of the microstructure quantification framework described above is first evaluated critically on synthetic microstructures obtained with a priori known and controlled grain shape characteristics. Synthetic microstructures were generated for this study using the open-source software Dream.3D<sup>2</sup> [46], which allows the user to specify parameters controlling the size and shape distributions of the microstructural constituents (i.e., grains in the present application). The Dream.3D algorithm for the synthetic generation first seeds ellipsoids and subsequently adjusts iteratively their shapes and positions to fill up the allocated volume, while trying to match the user-specified size and shape characteristics as closely as possible [47].

In this study, Dream.3D was employed for creating microstructures with various grain morphologies. Dream.3D only generates 3-D volume elements, whereas our focus in this study is on the analysis of 2-D maps generated by most of materials characterization equipment. To obtain 2-D microstructures from Dream.3D, we first generated 3-D representative volume elements (RVEs) with some out-of-plane thickness  $(255 \times 255 \times 65 \text{ voxels})$  and then extracted 2-D middle sections normal to the out-of-plane direction (z axis). For synthetic generation, the following classes of microstructures (inspired by those encountered in real metal samples) were considered: (i) equiaxed grains (e.g., annealed metal), (ii) coexisting small and large grains (e.g., partially recrystallized metal), and (iii-iv) pancake-shaped grains along the x and y directions (e.g., deformed metal). Microstructures of these classes were obtained using different sets of input parameters selected to achieve the targeted morphologies. Specifically, precursor ellipsoids with equal axes were used for equiaxed microstructures, whereas 10:1:1 ratios between the major axis and the two minor axes were assigned for microstructures with elongated grains. The microstructures with bimodal (duplex) grain size distributions were generated as pseudo composites consisting of phases with equivalent crystal structures but two distinct

<sup>&</sup>lt;sup>2</sup> Open source https://github.com/BlueQuartzSoftware/DREAM3D.

size distributions. For all RVEs, the identical equivalent grain diameter (based on the notion of an equivalent sphere) was targeted during generation.

The 2-D EBSD maps obtained in Dream.3D were analyzed using the open-source MTEX toolbox<sup>3</sup> [48,49] in MATLAB. Specifically, MTEX was used to segment the spatial orientation data with the misorientation angle threshold of 5° to obtain grains and their boundary segments. Grain boundary segments were then used as input for the algorithm of AR-CLD calculation as described in Section 2.3. Calculations of AR-CLDs were carried out with the aid of the *matrix-based* approach by placing test lines with a spacing equal to the grid step size in the synthetic EBSD maps and by sampling the whole range of directions,  $\theta \in [0^{\circ}, 180^{\circ})$  with a 1° step.

Fig. 4 shows exemplar EBSD maps of (i)-(iv) grain morphology classes generated in Dream.3D and their corresponding AR-CLDs as well as traditional characteristics of the grain size and shape. The conventional grain size measure based on the mean grain diameter (discussed in Section 1) was computed for all the generated microstructures. The calculated values indicate that all four synthetic EBSD maps have very similar mean grain diameter, in accordance with the values of the equivalent sphere diameter input into the Dream.3D code for the generation of these microstructures. It means that these different microstructures would be nearly indistinguishable in terms of the mean grain diameter used frequently in literature. Salient details about such microstructures and their differences can be revealed through distributions of the size and shape metrics (Fig. 4c). For example, extending the analysis of the grain diameter from the mean only to its distributions allows for identifying one predominant mode in the equiaxed microstructure and more than one mode in the bimodal microstructure (i-ii). For microstructures with non-equiaxed grains (iii-iv), one could get more insight by fitting grains into equivalent ellipsoids, which allows for analysis of aspect ratios and inclination angles between one of the sample directions and the major axes of the ellipsoids. Specifically, large mean aspect ratios indicate the elongated shape of the grains. whereas distribution of inclination angles (in respect to x axis) shows the expected preferential alignment of pancake shaped grains nearly parallel to the x and y axes of (iii-iv) microstructures, respectively.

The previous exercise shows that studying the size and morphology aspects of the microstructures requires separate analyses and representations, whose choice depends on the nature of the microstructure. At the same time, it is seen that all these microstructural characteristics can be readily captured in AR-CLDs and intuitively represented by their polar visualizations (Fig. 4b). Indeed, the microstructure with equiaxed grains is represented by a circular pattern of high AR-CLD intensity, whose radius corresponds to the most probable chord length. The radius of high-intensity ring is equal in all directions of the microstructure, which indicates the statistical morphological isotropy. The AR-CLD obtained for the microstructure with populations of smaller and larger grains also has an axisymmetric pattern but with two rings of high probability that signifies the presence of two modes in the CLD. The microstructures with pancake-shaped grains have AR-CLDs with characteristic elliptical patterns, oriented according to the preferred alignment of the grains. It is seen that these elliptical patterns are slightly deviated from a perfect alignment with the corresponding sample axes, which resulted from the stochastic nature of microstructure generation in Dream.3D. These deviations also agree with the modes in inclination angle distributions shown in (Fig. 4c) equal to 178.9° (instead of ideal 0° or 180°) and 87.3° (instead of ideal 90°) for (iii) and (iv) microstructures, respectively.

This example illustrates that AR-CLDs alone capture the essential information on the size, shape, and preferred spatial alignment of the grains. Furthermore, all these features are easily inferred from the polar visualizations of AR-CLDs, which facilitates distinction, and both

qualitative and quantitative comparison of microstructures. We finally note that the computational algorithms and protocols for AR-CLDs were identical for all four microstructure classes considered, and did not require prior knowledge on the grain structure type.

In addition to statistical description and intuitive visual representation, it is often of interest to obtain a low-dimensional representation of microstructures for quantification, specification, and use in models. Mean grain diameter is a scalar description widely used for these purposes. We first note that if an averaged measure is required, the mode of CLD can be readily computed by its averaging over sampling directions (i.e.,  $\theta$  angles) and finding the chord length corresponding to the maximum value of the averaged CLD. Mean chord length can be also obtained during CLD calculations, Alternatively, PCA of AR-CLDs of an ensemble of microstructures can be carried out for obtaining low-dimensional representation as introduced in Section 3. To test and demonstrate the use of PCA on AR-CLDs, we generated a series of 30 synthetic EBSD maps of four classes: 10 equiaxed, 10 bimodal, 10 pancake-shaped with five of them aligned along the x axis and five of them aligned along the y axis. To obtain several maps within each class, generation was performed multiple times with the same input statistics as each run of Dream.3D produces a similar but unique instantiation of the targeted microstructure. For each synthetic EBSD map, AR-CLD was calculated as described above. PCA was then performed on the set of AR-CLDs which yielded 30 basis maps or patterns (equal to the number of the samples in the ensemble) sorted according to their explained variance. The virtue of PCA is that only few of them are often sufficient to capture a large portion of the variance. For our synthetic dataset, the first three principal components (whose bases are shown in Fig. 5a) collectively explain 96.5% of variance in the dataset as seen in Fig. 5c. It follows then that the first three scalar PC scores (or weights of the first three patterns) can be used for low-dimensional representation of the microstructures. The fact that the first three principal components carry essential details of AR-CLDs can be seen in Fig. 5d, where AR-CLD calculated for one of the microstructures in the ensemble is compared against the reconstructed AR-CLD using Eq. (7) with only the first three principal components (i.e., with R=3). It is evident that the reconstructed AR-CLDs has all the salient features of the original AR-CLD: the presence of a bimodal distribution in the CLD, the corresponding chord lengths, and morphological isotropy. Fig. 5b depicts the low-dimensional representation in terms of the first three PC scores (or weights of AR-CLD patterns represented by basis maps), in which each symbol corresponds to a microstructure of the ensemble. It is seen that EBSD maps corresponding to the four microstructure classes are clearly clustered in the PCA space signifying the similarity of the microstructures within a cluster in terms of their AR-CLDs. This clustering is obtained purely as a result of PCA in an unsupervised fashion, i.e., without any prior labeling of the microstructures belonging to different classes. Such low-dimensional representations can be thus used for classification and comparison of polycrystalline microstructures, as a result of various processing histories, for example.

The properties of PCA also allow a meaningful interpretation of the observed clustering by inspection of the corresponding basis maps (shown in Fig. 5a). For such interpretations, one starts with the ensemble-averaged statistics and systematically adds the features in each basis map, one at a time. In doing so, it is important to recognize that each basis map has both positive and negative values. For instance, as one proceeds along PC1, the red colored elements of the PC1 basis map are added and the blue colored ones are removed, where the color intensity reflects the actual amounts removed or added. Therefore, it should be clear that as one moves along the positive PC1 direction, one is adding equiaxed components at the smaller length while removing the equiaxed components at the higher length as well as the x- and ypancake components. Similarly, the PC2 basis map adds y-pancake components and removes x-pancake components, as one moves along PC2 axis. In general, higher-order principal components add more complex features compared to the lower-order principal components.

<sup>&</sup>lt;sup>3</sup> Open source https://mtex-toolbox.github.io/.

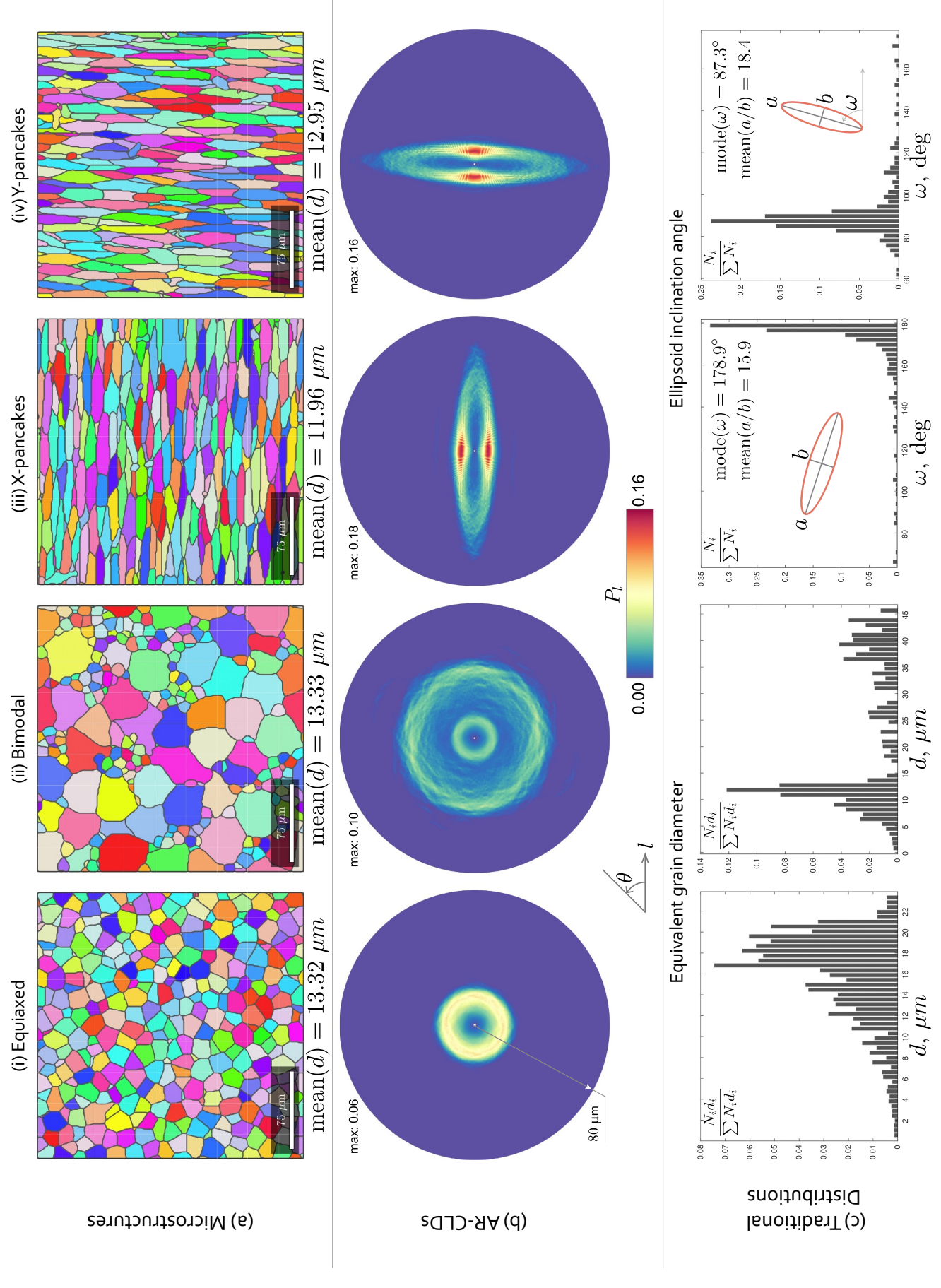


Fig. 4. Synthetic EBSD maps (a), their corresponding AR-CLDs (b), and classical distributions of grain diameter and the inclination angle of equivalent ellipsoids (c). The AR-CLDs were obtained with the bin size of  $\Delta l = 1 \ \mu m$ .

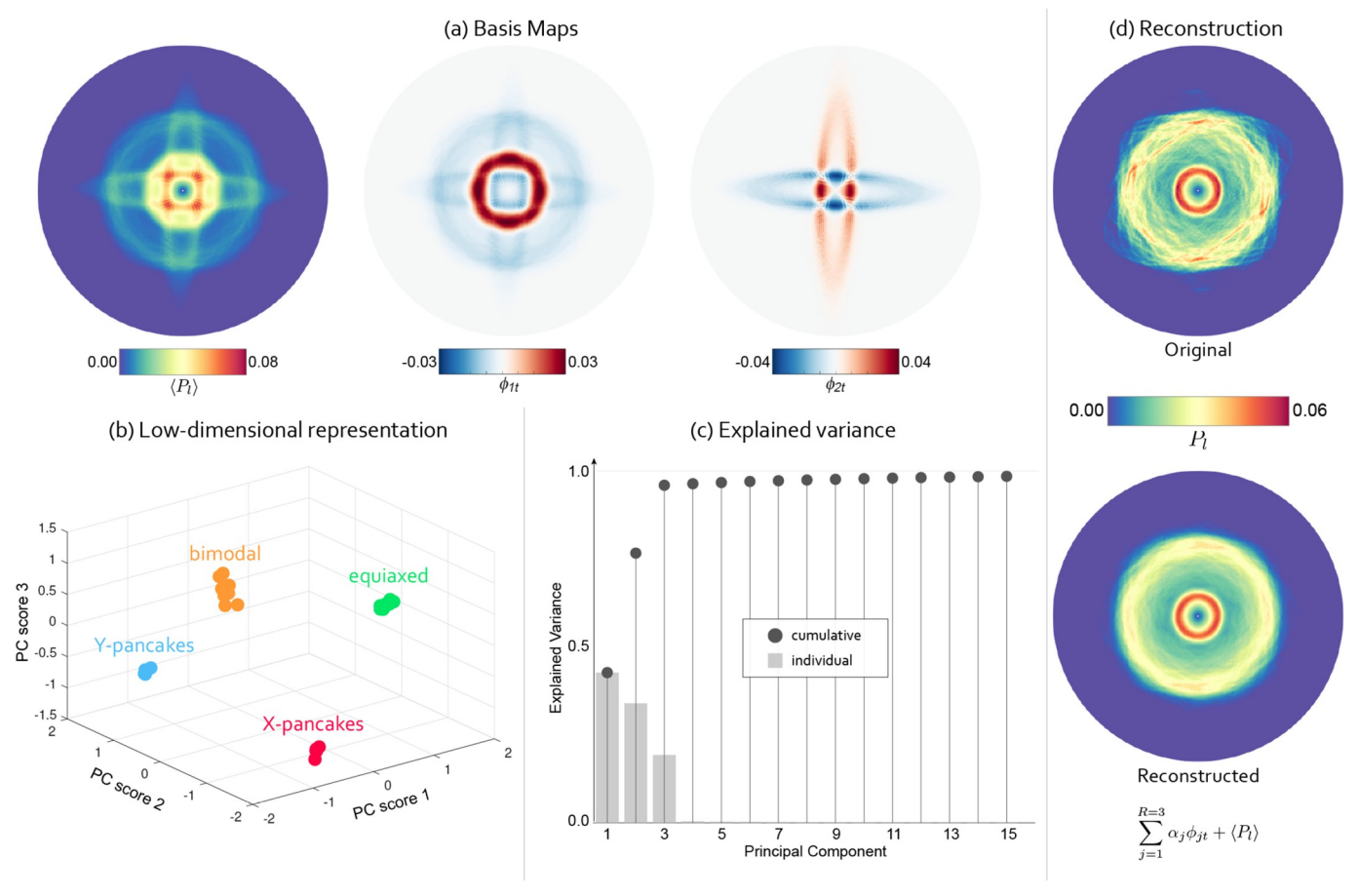


Fig. 5. Results of principal component analysis of AR-CLDs of an ensemble of 30 synthetic microstructures consisting of equiaxed, bimodal, and pancake-shaped grains: (a) ensemble-average AR-CLD and two first patterns (or basis maps) corresponding to the most variance in AR-CLD of the ensemble, (b) low-dimensional representation of AR-CLDs of the ensemble shown as 3-D projection of the PCA space in terms of the first three PC scores (corresponding to the shown basis maps), (c) variance captured (individually and cumulatively) by first 15 principal components (with first three of them explaining 96.5%), (d) illustration of reconstruction of AR-CLD of a microstructure in the ensemble using first three principal components.

These observations demonstrate the tremendous benefits of orthogonal representations (e.g., obtained by PCA) in seeking low-dimensional visualizations. The quantification framework for synthetic microstructures presented here is expected to be of significant value in validation of synthetically generated RVEs that are statistically equivalent to the experimentally observed microstructures, essential for many multiscale materials modeling efforts [47,50].

# 4.2. Experimental Datasets

Our next case study aimed at quantification of experimentally measured microstructures of metallic samples. As a specific example, we considered Ni-base superalloys used for turbine disks [51]. These Ni-base superalloys are typically produced by powder metallurgy routes that include isothermal forging and annealing as a final thermo-mechanical operation. The annealing step results in formation of annealing twins and, in some cases, in preferential grain growth leading to bimodal grain size distribution. Annealing twins play an important role in the performance of the superalloys in service. On one hand, twins serve as effective barriers to dislocation slip [52-54] and increase the yield (or flow) strength of the material. On the other hand, in the absence of extrinsic defects (e.g., pores), annealing twins often serve as sites for crack initiation [55-58] and significantly affect the fatigue life, a limiting factor for the deployment of the alloys in service. Consequently, a rigorous quantification of microstructures with annealing twins is important for this application. As twin morphology usually differs from that of parent grains (whose shapes are also altered by the traversing

twins), detecting preferred shape and the morphological orientation of constituents induced by the presence of twin boundaries (of different length fractions) is of special interest. These microstructure characteristics, while not apparent from such common metrics as the grain diameter, are significant based on observations of strain localization and fatigue crack initiation along long twin boundaries in grains favoring localization [59–61].

With this motivation, we consider two superalloys, IN100 and René 88DT [62], whose microstructures were previously studied in relation to fatigue crack initiation [60]. These superalloys had different grain size distributions and different fractions of annealing twin boundaries. Here we analyze microstructures of both alloys (exemplified in Fig. 6a) in terms of AR-CLDs calculated on EBSD maps of four regions in both IN100 and René 88DT (acquired as described in [60]). Grains were segmented based on a threshold misorientation angle of 5°, whereas annealing twin boundaries were identified as the boundaries with misorientations of 60° around <111> crystal axes and tolerance of 5° [63]. For each EBSD map, AR-CLDs were computed twice: once considering all boundaries (including twin boundaries) and once ignoring the twin boundaries. Since these experimental EBSD maps had a substantial number of grain boundary segments, AR-CLDs were computed using sequential algorithm for obtaining chord lengths by placing test lines with a spacing equal to the EBSD grid step in the complete range of directions,  $\theta \in [0, 180]$ , with a 1° step. Chord length statistics obtained in four different regions of the same sample were combined to provide better sampling for AR-CLDs in each case (with and without twin boundaries).

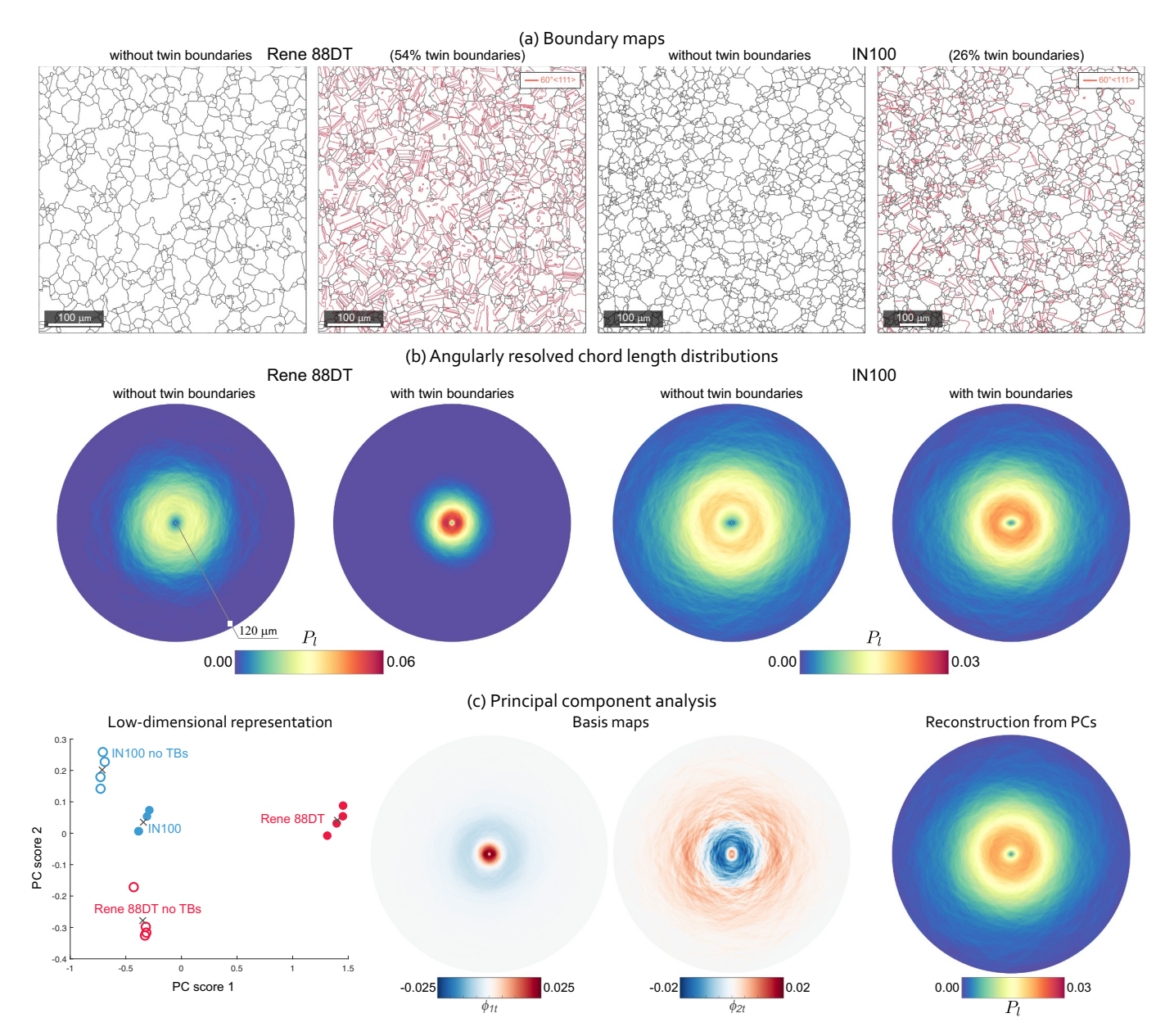


**Fig. 6.** Quantification of experimentally measured grain structures of IN100 and René 88DT: (a) grain and twin boundaries extracted from EBSD maps of IN100 and René 88DT and (b) their AR-CLDs with and without consideration of twin boundaries; (c) principal component analysis results including low dimensional representation, first two basis maps, and AR-CLD of IN100 with twin boundaries reconstructed using first two principal components. The AR-CLDs were obtained with the bin size of Δl = 1 μm.

The results obtained with and without considering twin boundaries in the two alloys reveal interesting features of the grain morphology and the effect of the twin boundaries on AR-CLD (Fig. 6b). First, when twin boundaries are considered, the peak intensities in the AR-CLD of René 88DT correspond to shorter chords compared to those in the AR-CLD of IN100 in agreement with the smaller grain diameter in René 88DT reported earlier (43  $\mu m$  vs. 26  $\mu m$  [60]). The AR-CLD of IN100 also exhibit non-zero intensities in a wider range of chord lengths compared to AR-CLD of René 88DT, which captures the presence of a number of large grains seen in IN100 boundary map (i.e., bimodal size distribution). In addition, it is seen that both microstructures are, for the most part, morphologically isotropic with and without twin boundaries. Given a number of high-aspect ratio regions surrounded by twin boundaries seen in the maps (Fig. 6a, especially for René 88DT), the overall axisymmetry of AR-CLDs (considering twin boundaries) indicate the absence of preferred morphological orientation of annealing twins.

Further interesting observations can be made from the comparison of AR-CLDs of all boundaries against AR-CLDs neglecting the twin boundaries for the two alloys. It is seen that, in IN100, twin boundaries (constituting 26% boundary length fraction) have a minor effect on the AR-CLD with only a slight increase of probability of short chord lengths while keeping the overall distribution very similar to that obtained without twin boundaries. In contrast, the effect is much more dramatic in René 88DT with 54% twin boundary length fraction, where non-zero probability shifts from chord lengths of 10-50 µm to 2-18 µm range (compare AR-CLD maps for René in Fig. 6b). These results indicate how the large fraction of annealing twin boundaries in René 88DT significantly shortened, in the statistical sense, chords in the microstructure. However, the fraction of 26% annealing twin boundaries in IN100 was insufficient for such statistically significant changes in the AR-CLDs. As in the previous case study, all these observations – on the grain size and morphology, the modality of the size distribution, and the effect of twin boundaries on CLDs - are made by intuitive

interpretation of AR-CLD maps. These insights would have otherwise required analysis of multiple traditional size and morphology measures or distributions.

To complete the analysis, we apply PCA to get low-dimensional representation of the AR-CLDs for the experimentally measured microstructures (Fig. 6c). High-fidelity low-dimensional representation of microstructures with bimodal grain size distributions (e.g., IN100 with twin boundaries) is of special interest because they cannot be well represented by commonly used mean grain diameter and standard deviation that assume Gaussian (or normal) distribution of the grain diameter (with a single mode) [28]. To carry out PCA, two AR-CLDs (with and without twin boundaries) for each of the four regions of each alloy were calculated and considered separately, which provided 16 AR-CLDs in total. The low-dimensional representation of these 16 AR-CLDs in terms of the first two PC scores (Fig. 6c) features four distinct clusters that correspond to (i) René 88DT with twin boundaries, (ii) René 88DT without twin boundaries, (iii) IN100 with twin boundaries (iv) IN100 without twin boundaries. Clustering of the AR-CLDs from four different regions close to the combined AR-CLDs of each alloy (marked by crosses in Fig. 6c) indicate small variations of the grain size morphology between the studied regions. The corresponding basis maps show how these principal components capture different modes in the AR-CLDs. Finally, it is seen that, for this dataset, the first two principal components (capturing 96% variance) suffice for a meaningful reconstruction of the original AR-CLDs (Fig. 6c) even with bimodal AR-CLD obtained for IN100 with twin boundaries. AR-CLDs and their low-rank representations obtained by PCA therefore provide for a versatile framework for quantification and representation of microstructures with diverse grain size and shape distributions, including those observed experimentally. One of the potential applications of this framework (particularly in the context of Ni-base superalloys with twin boundaries) is assessing the statistical equivalence (or difference) of microstructures with non-trivial size distributions of the constituents ensuing from complex processing paths.

### 4.3. Simulation Datasets

We further tested our quantification framework, and its scalability in particular, on a computational dataset of microstructure evolution during static recrystallization. Static recrystallization is a phenomenon frequently observed in heavily deformed metals during which the deformed microstructure is swept by nucleation and subsequent growth of recrystallizing grains [64]. The deformed microstructure is primarily

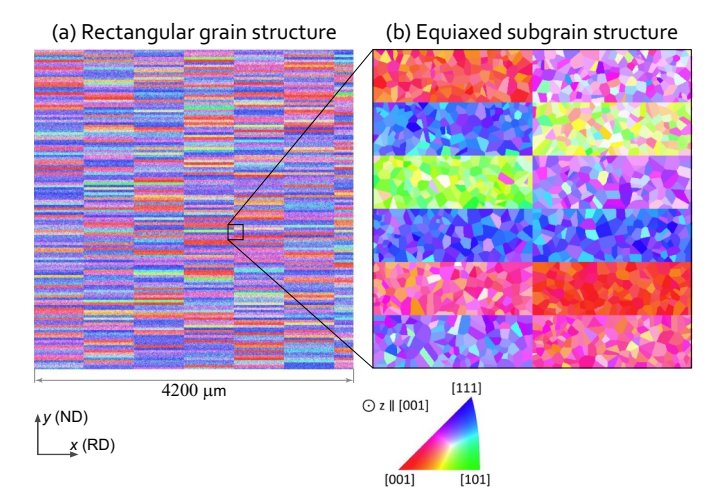


Fig. 7. The initial configuration of the 2-D synthetic microstructure for recrystallization simulations built as a polycrystalline aggregate of rectangular parent grains (a) with aspect ratio of 20:1 subdivided into equiaxed subgrains (b). The total number of subgrains is  $9.83\times10^6$ .

constituted by subgrains, i.e., grains possessing predominantly lowangle rather than high-angle boundaries, which are known to act as nuclei for primary static recrystallization, especially in high-stacking fault energy f.c.c. alloys [64]. Understanding and predicting microstructure evolution during recrystallization is of engineering interest because the recrystallized microstructure significantly differs from the initial deformed one (both in terms of crystallographic texture and grain morphology) with strong dependence on the thermo-mechanical conditions as well as an impact on the properties and their anisotropy. One of the key challenges in such predictions is that successful nucleation during recrystallization belongs to a class of rare events as only each thousandth candidate subgrain, if at all, has a substantial advantage to evolve into a recrystallized grain consuming the others. Obtaining statistically significant data on such rare events and their dependence on the process variables demands monitoring myriads of candidate sites under controlled conditions, which requires a combination of experimental and computational studies. The computational tools aiming for statistical significance yield massive microstructure data which in turn require efficient approaches to microstructure analysis. In addition to large population sizes, microstructural evolution during recrystallization can be morphologically anisotropic with multimodal size distributions of the constituents. The datasets on recrystallizing microstructures therefore provide for a unique opportunity to test the quantification framework presented in this work.

The detailed descriptions of the computational approach utilized in the present study and the microstructural setup were reported previously [65]; only the essential details of these simulations are reiterated here. The simulations were executed with the open source OpenMP-parallelized GraGLeS model<sup>4</sup> solver [37] with the objective to follow the preferential evolution of a large number of individual subgrains within their neighborhood during isothermal annealing of cold-rolled Fe–2.4%Si non-grain-oriented steel. The driving force for subgrain growth was considered to originate from capillary effects and the difference in the dislocation density across subgrain boundaries.

The initial microstructure was synthesized based on experimental data (on grain orientations, shapes, and dislocation density) available for the steel after cold rolling to 70% thickness reduction [66]. The subgrain structure was constructed using a hierarchical Poisson-Voronoi tessellation<sup>5</sup> First, 10,000 rectangular parent grains (with 20:1 aspect ratio) were instantiated (Fig. 7a), followed by their synthetic subdivision into 1000 equiaxed subgrains each so that the initial microstructure contained 9.83 million equiaxed subgrains (Fig. 7b).

The described simulations allowed continuous monitoring of the microstructure evolution, including subgrain area, topology, and the geometry of subgrain boundaries. For the purposes of the present study, the subgrain boundary contours were written to file each 100th integration step. Note that during the simulated recrystallization process, the fraction of high-angle boundaries tend to increase, which makes the classical conceptual distinction between "grains" and "subgrains" potentially too simplified so that we continue to refer to them as subgrains and consider all boundaries in the analysis. The contour points of subgrain boundaries exported during the simulations were paired to constitute boundary segments for the AR-CLD analysis. Since the datasets contained extremely large numbers of boundary segments (up to tens of millions per time step), sequential approach was utilized with trivial parallelization of CLD calculations in different directions. In addition, the subgrain boundary map at the first studied time step (T = 500), which contained the largest number of boundary segments, was split into four sub-domains analyzed separately with subsequent merging of the chord length statistics. The AR-CLDs were computed for subgrain boundaries obtained at different time steps of the simulations considering the entire range of directions,  $\theta \in [0, 180)$ , with a 1° step

<sup>&</sup>lt;sup>4</sup> Open source https://github.com/GraGLeS.

<sup>&</sup>lt;sup>5</sup> Open source https://github.com/GraGLeS/IMM\_MicrostructureGenerator.

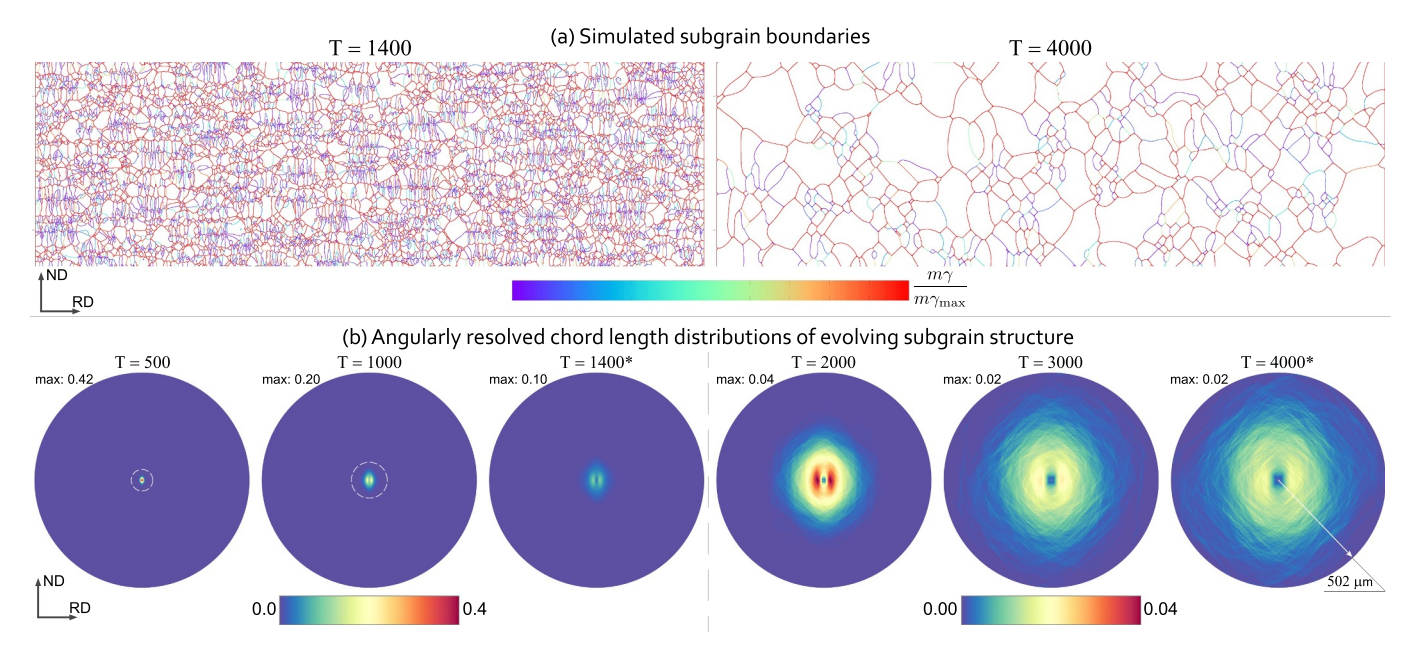


Fig. 8. Summary of the results of the recrystallization case study: (a) partial subgrain structure renderings at two time steps, T, of the recrystallization simulation illustrating the predicted subgrain growth (the corresponding AR-CLDs in (b) are marked with asterisks); (b) AR-CLDs obtained for the subgrain structure at different time steps, T, with the bin size of  $\Delta l = 3.36 \,\mu\text{m}$ .

and at least 500 test lines for each direction.

Fig. 8 distills results of the simulations predicting the subgrain structure evolution and the corresponding AR-CLD calculations. The predicted subgrain growth, exemplified by subgrain boundary maps at two time steps in Fig. 8a, is clearly captured in the corresponding AR-CLDs (Fig. 8b). Indeed, one can see significantly higher probabilities of finding short chords at the early stages compared to AR-CLDs later in the process that reflect more distributed probabilities of chords in a wide range of lengths.

An interesting observation in the AR-CLDs is the anisotropic probability pattern seen in the AR-CLDs (Fig. 9) corresponding to the early stages of recrystallization, which was inherited, to a certain degree, to the end of the studied time interval (Fig. 8b). Indeed, the peak probability in AR-CLD corresponds to small chords (<  $10\,\mu m$ ) along the rolling direction (RD, parallel to x axis), whereas the probability of chords of the same lengths in the normal direction (ND, parallel to y axis) is lower. This lower probability of small chords along ND is compensated by the presence of chords in a wider range of lengths (up to  $30\,\mu m$ ).

The anisotropic pattern of non-zero probability in AR-CLD indicates the non-equiaxed shape of subgrains with some elongation in ND. It is a surprising observation because subgrains in the initial microstructure

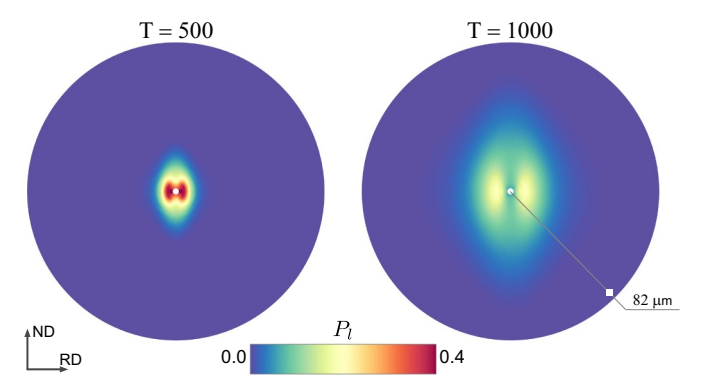


**Fig. 9.** Close-up of AR-CLD patterns at T = 500 and T = 1000 (their locations in Fig. 8b are indicated with dashed circles, chord length ranges are shown with arrows).

were generated equiaxed (Fig. 7b), which was expected to lead to relatively isotropic growth. The observations made with AR-CLDs, however, suggest that, as soon as the structure starts to evolve, the net subgrain boundary migration progresses differently in the principal directions (and particularly in RD vs. ND).

While anisotropic growth was observed in classical experiments on recrystallization in single- and bi-crystals [67] and attributed to inclination-dependent grain boundary mobilities, the present morphological anisotropy detected with AR-CLDs originated in part from the synthetic microstructure instantiation. Particularly, we attribute the transient subgrain shape anisotropy to differences in the dislocation content and disorientation between adjacent subgrains. First, for a randomly picked subgrain pair, the difference in the driving force is likely to be higher when the two subgrains belong to different parent grains compared to neighboring subgrains within the same parent grain. Second, by design, subgrains within the same parent grain have lower disorientation to each other on average compared to their neighbors in adjacent parent grains. Both contributions act concomitantly causing multiple subgrains to migrate farther in the direction of the neighboring parent grain (i.e., ND) than in the elongation (or major axis) direction of parent grains (i.e. RD).

We conclude our examination in this case study with PCA of the AR-CLDs obtained for subgrain structures at 44 time steps  $(T = \{500,1000,1100,...,5200\})$  of the recrystallization simulation. Fig. 10a depicts the results of PCA of these 44 AR-CLDs shown in terms of the time evolution of the first three PC scores that collectively capture 98.7% variance in the AR-CLDs. This representation effectively captures substantial changes in the subgrain scale structure during the transient between the deformed and the recrystallized states in the early stages of the process as well as the decrease in the rate of evolution towards the end of the simulated time period.

The basis maps (Fig. 10b) identify the main changes in the AR-CLDs during the recrystallization process. For example, the pattern of minimum (negative) values in the first basis map resembles the pattern of high intensity of AR-CLD at the beginning of the process (T=500). Accordingly, the first PC basis indicates negative values for the very short chords (in all directions), and relatively small positive values for the larger chords (again in all directions). Therefore, an increase in the first PC score captures a loss of these short chords and a very small

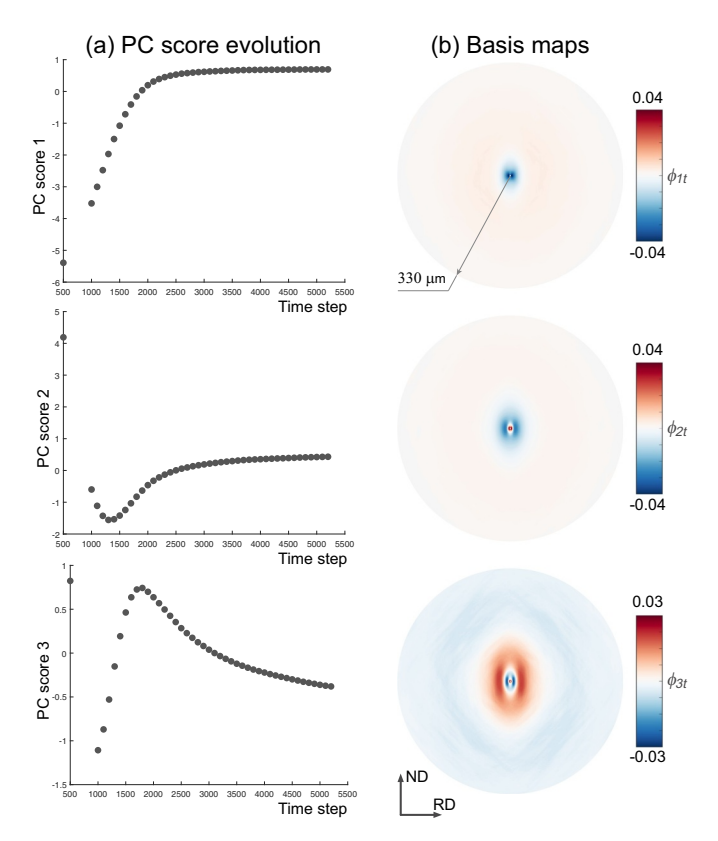


**Fig. 10.** Results of the principal component analysis shown in terms of (a) the time evolution of the first three PC scores and (b) the corresponding basis maps.

increase in the distribution of the larger chords. The other two PC scores and bases similarly capture the salient changes in AR-CLD at different stages of the microstructure evolution. Finally, it is interesting to note that the PC1 and PC2 scores asymptote with time, indicating that the corresponding changes in AR-CLD are complete. At the same time, the PC3 score has not yet reached a steady-state value, suggesting that the corresponding changes are not yet complete. These are likely signatures of a continuing transition from the regime controlled by the difference in stored elastic energy to that dominantly driven by capillarity, which is expected within the classical sequence of static recrystallization followed by the stage of grain growth.

The results demonstrate the successful application of the present framework to recrystallization simulation datasets with tens of millions of boundary segments. In the absence of the proposed framework, the simulation output on subgrain morphology and size would have been likely discussed qualitatively by visual inspection or solely in terms of the grain diameter, thereby missing finer details of the subgrain size and shape evolution as identified in the present case study. The results are of immediate value both for improved interpretation of simulation results and for guiding synthetic microstructure generation. Indeed, the idealized shape and size equality of the parent grains used for building the initial microstructure was found to affect the geometrical path along which the subgrain structure evolves. The latter indicates the need in improved microstructure generators that aim not only at higher grain shape variety, which tools like Dream.3D already offer, but especially at more efficient scaling solutions. These solutions could provide extremely large RVEs for simulations that capture rare events such as nucleation during static recrystallization.

#### 5. Discussion

In this work, we presented a grain boundary-based approach for fully automated calculations of AR-CLDs for digital microstructures, and demonstrated their application to quantification and representation of polycrystals with diverse grain morphologies and size distributions. It was shown through the case studies that AR-CLDs capture important morphological details that may be otherwise overlooked by metrics such as the mean grain diameter. It was also demonstrated that polar visualizations of AR-CLDs provide for intuitive representation of grain structures, from which the range of chord lengths (related to grain size), their distribution (e.g., unimodal vs. multimodal), the shape (e.g., equiaxed vs. non-equiaxed) and the preferred alignment of grains can be all readily inferred from a single plot.

We envision that the presented approach is especially suitable for incorporation into routine post-processing of EBSD datasets. The MATLAB code developed for AR-CLD in this work is open-sourced and made available to the community on GitHub. 6 The code is compatible with open-source MTEX toolbox, which is being actively developed and increasingly adopted for EBSD and texture analysis. Other EBSD postprocessing software can be also used for exporting boundary segments from which AR-CLDs can be calculated as described in Section 2.3. For many practical situations of EBSD analysis, the presented implementation is quite efficient as seen in the summary of the CPU times needed for AR-CLD computations (Table 1). AR-CLDs in all directions with a 1° step for a typical EBSD map took 1-6 min on a personal computer. We note that these CPU times are reported for AR-CLD calculations with a large number of test lines placed at each EBSD pixel (i.e., spacing equal to EBSD grid step). Such dense sampling was adopted for making full use of all the information available in the EBSD map, which is motivated by high cost of the experimental data. Of course, the users can opt to reduce the number of scan lines to reduce the CPU time as needed for their specific application. Relevant to the computational cost, we also demonstrated that two algorithms can be employed depending on the situation: (i) matrix-based (no loops over test lines) for the cases of moderate size boundary maps and/or abundance of memory, (ii) sequential looping over test lines for large maps and/or limited memory. The algorithms for large microstructure maps can be further accelerated by parallelized computations owing to the independence of CLD calculations in different directions. In future studies, further acceleration can be explored by streaming instructions for CPUs or, even more efficiently, for GPUs, which will be especially important for potential extensions of the present approach to 3-D microstructures.

We have also shown that PCA can be successfully applied on AR-CLDs when low-dimensional measures of microstructure descriptions are sought. Typically low-dimensional representations are obtained by averaging statistical distributions, e.g., mean grain diameter. The virtue of PCA as an alternative to averaging is that it allows for identification of salient features in terms of which microstructure features vary the most in the given ensemble. In addition, a few principal components often suffice for meaningful reconstruction of the original AR-CLD regardless of the distribution type (including bimodal, anisotropic, etc.), which is not always the case using conventional Gaussian metrics (i.e., mean and standard deviation). In addition to efficient representation, PC scores of AR-CLDs can serve as succinct and robust descriptors of the grain structure and thus facilitate the formulation of quantitative processing-structure-property relationships. Our prior research has already shown the potential of such microstructure representations for establishing processing-structure [33] and structure-property relationships using emerging data science strategies [34-36]. A potential application of the present quantification framework is the development of statistical data-driven models that capture a microstructure-property relationship (e.g., yield strength) as a function of PC scores of AR-CLD. The potential advantage of such statistical models as compared to classical ones (e.g., Hall-Petch relationship) is that the combined effects of grain size, shape, and their alignment captured in AR-CLDs (but

<sup>&</sup>lt;sup>6</sup> Repository address: https://github.com/mined-gatech/AR-CLD-bnd.

Table 1
Wall-clock CPU times for the case studies carried out on a 4.2GHz desktop with 16GB RAM. Synthetic case study was performed using *matrix-based* approach with 1 CPU, *sequential* approach was used for the rest of the case studies employing trivial MATLAB parallelization with 4 CPUs. The CPU times are shown for AR-CLD calculations only excluding I/O operations.

Dataset	# Segments	# Test lines	CPU time
Synthetic René 88DT without TBs René 88DT with TBs IN100 without TBs IN100 with TBs REX (T = 5000)	$1.2 \times 10^{4}$ $3.8 \times 10^{4}$ $8.3 \times 10^{4}$ $1.9 \times 10^{5}$ $2.3 \times 10^{5}$ $3.8 \times 10^{4}$	≥ 250 ≥ 625 ≥ 625 ≥ 1800 ≥ 1800 ≥ 500	56 s 28.5 s 47.0 s 3.9 min 5.4 min 25.9 s
ReX (T = 3000) ReX (T = 2000) ReX (T = 1400) ReX (T = 1000) ReX (T = 500)	$7.4 \times 10^{4}$ $2.2 \times 10^{5}$ $1.2 \times 10^{6}$ $5.8 \times 10^{6}$ $1.2 \times 10^{7}$	≥ 500 ≥ 500 ≥ 500 ≥ 500 ≥ 500	38.7 s 1.4 min 7.4 min 32.4 min 49.0 min

overlooked by grain diameter) can be accounted in the microstructure–property relationship.

While our focus in this work was on mesoscale microstructure quantification of polycrystalline metals, the approach is sufficiently abstract and versatile to be utilized at other length scales as well as on other material systems. Such versatility was achieved by formulating the approach based on boundary segments defined by the coordinates of their end points without any restriction to them being boundary segments of grains in metals. The presented ideas can be therefore adopted by communities focused on other material systems, such as geological [3] and biological materials, food [68], and other systems, in which the size and morphology of constituents are of interest.

#### 6. Conclusions

In this work, we have presented a framework based on angularly resolved chord length distribution (AR-CLD) and principal component analysis (PCA) for quantification of polycrystalline mesostructures with the following conclusions.

- 1. AR-CLDs can be calculated based on algorithms for finding intersection points between arrays of line segments, i.e., test lines and grain boundary segments defined by continuous coordinates of their end points
- 2. From the case study on synthetic microstructures, we demonstrated that AR-CLDs capture differences in both size and shape characteristics of predominantly equiaxed and elongated grains with alignment in different directions as well as the character of the size distribution (unimodal, duplex/bimodal, etc.). In addition to intuitive polar visualization of AR-CLDs, these different microstructures can be efficiently represented by principal components of AR-CLDs obtained by PCA.
- 3. The AR-CLD analysis of the effects of annealing twin boundaries on grain shape and morphology revealed (i) the absence of preferential alignment of twin boundaries in the microstructure, (ii) a small effect of 26% annealing twin boundaries in IN100 and significant effect of 54% annealing twin boundaries in René 88DT on chord length distribution, (iii) successful low-dimensional representation of microstructures containing annealing twins using principal components of AR-CLDs that allows for comparison of experimentally measured microstructures with various grain size and shape distributions.
- 4. The analysis of evolving subgrain boundary networks predicted by recrystallization simulations demonstrated scalability of the presented algorithm for AR-CLD calculations, allowed detection of morphologically anisotropic subgrain growth and its quantitative description in terms of principal components of AR-CLDs as well as

identified potential for improvements in computational recrystallization studies by reducing biases introduced in synthetic microstructure generation.

#### Acknowledgments

The authors gratefully acknowledge the support by their respective funding agencies and grants: MIL – National Science Foundation (United States) NSF grant #1664172 SI2-SSI:LIMPID: Large-scale IMage Processing Infrastructure Development; MK – the German Research Foundation (Germany) DFG grants GO335/44-1 and BA4253/2-1; IJB – the Office of Naval Research under contract N00014-17-1-2810; LST – the French State through the program Investment in the Future operated by the National Research Agency (France) (ANR) and referenced by ANR-11-LABX-0008-01 (LabEx DAMAS); TMP – NSF grant #1650972 EAGER: Collaborative 3D Materials Science Research in the Cloud; SRK - the Office of Naval Research (United States) ONR grant N00014-15-1-2478.

#### **Data Availability**

The raw/processed data required to reproduce these findings cannot be shared at this time as the data also forms part of an ongoing study.

#### References

- D.T. Fullwood, S.R. Niezgoda, B.L. Adams, S.R. Kalidindi, Microstructure sensitive design for performance optimization, Prog. Mater. Sci. 55 (6) (2010) 477–562, https://doi.org/10.1016/j.pmatsci.2009.08.002.
- [2] R. Bostanabad, Y. Zhang, X. Li, T. Kearney, L.C. Brinson, D.W. Apley, W.K. Liu, W. Chen, Computational microstructure characterization and reconstruction: review of the state-of-the-art techniques, Prog. Mater. Sci. 95 (2018) 1–41, https://doi.org/10.1016/j.pmatsci.2018.01.005.
- [3] A.J. Schwartz, M. Kumar, B.L. Adams, D.P. Field (Eds.), Electron Backscatter Diffraction in Materials Science, Springer, Boston, MA, 2009, https://doi.org/10. 1007/978-0-387-88136-2.
- [4] B.L. Adams, S.R. Kalidindi, D.T. Fullwood, Microstructure Sensitive Design for Performance Optimization, Elsevier Science, 2012, https://www.sciencedirect. com/book/9780123969897/microstructure-sensitive-design-for-performance-optimization
- [5] U.F. Kocks, C.N. Tomé, H.-R. Wenk, Texture and Anisotropy: Preferred Orientations in Polycrystals and their Effect on Materials Properties, Cambridge University Press, Cambridge, UK, 2000, https://doi.org/10.1007/978-0-387-88136-2.
- [6] E. Hall, Variation of hardness of metals with grain size, Nature 173 (4411) (1954) 948.
- [7] N. Petch, XVI. The ductile fracture of polycrystalline  $\alpha$ -iron, Philos. Mag. 1 (2) (1956) 186–190.
- [8] B.S. Fromm, B.L. Adams, S. Ahmadi, M. Knezevic, Grain size and orientation distributions: application to yielding of α-titanium, Acta Mater. 57 (8) (2009) 2339–2348, https://doi.org/10.1016/j.actamat.2008.12.037.
- [9] S. Sun, V. Sundararaghavan, A probabilistic crystal plasticity model for modeling grain shape effects based on slip geometry, Acta Mater. 60 (13–14) (2012) 5233–5244, https://doi.org/10.1016/j.actamat.2012.05.039.
- [10] S. Berbenni, V. Favier, M. Berveiller, Micro-macro modelling of the effects of the grain size distribution on the plastic flow stress of heterogeneous materials, Comput. Mater. Sci. 39 (2007) 96–105, https://doi.org/10.1016/j.commatsci.2006. 02.019 (1 SPEC, ISS).
- [11] P. Lehto, H. Remes, T. Saukkonen, H. Hänninen, J. Romanoff, Influence of grain size distribution on the Hall-Petch relationship of welded structural steel, Mater. Sci. Eng. A 592 (2014) 28–39, https://doi.org/10.1016/j.msea.2013.10.094.
- [12] P. Lehto, J. Romanoff, H. Remes, T. Sarikka, Characterisation of local grain size variation of welded structural steel, Weld. World 60 (2016) 673–688, https://doi. org/10.1007/s40194-016-0318-8.
- [13] H. Bunge, F. Wagner, P. Van Houtte, A new way to include the grain shape in texture simulations with the Taylor model, J. Phys. Lett. 46 (23) (1985) 1109–1113.
- [14] G. Herzer, Grain size dependence of coercivity and permeability in nanocrystalline ferromagnets, IEEE Trans. Magn. 26 (5) (1990) 1397–1402.
- [15] M. Groeber, S. Ghosh, M.D. Uchic, D.M. Dimiduk, A framework for automated analysis and simulation of 3D polycrystalline microstructures. Part 1: statistical characterization, Acta Mater. 56 (6) (2008) 1257–1273, https://doi.org/10.1016/j. actamat.2007.11.041.
- [16] A.T. Polonsky, M.P. Echlin, W.C. Lenthe, R.R. Dehoff, M.M. Kirka, T.M. Pollock, Defects and 3D structural inhomogeneity in electron beam additively manufactured Inconel 718, Mater. Charact. (September 2017), https://doi.org/10.1016/j. matchar.2018.02.020.
- [17] L.S. Toth, S. Biswas, C. Gu, B. Beausir, Notes on representing grain size distributions obtained by electron backscatter diffraction, Mater. Charact. 84 (2013) 67–71, https://doi.org/10.1016/j.matchar.2013.07.013.

- [18] M. Fátima Vaz, M. Fortes, Grain size distribution: the lognormal and the gamma distribution functions, Scr. Metall. 22 (1988) 35–40, https://doi.org/10.1016/ S0036-9748(88)80302-8 (higher x).
- [19] S.P. Donegan, J.C. Tucker, A.D. Rollett, K. Barmak, M. Groeber, Extreme value analysis of tail departure from log-normality in experimental and simulated grain size distributions, Acta Mater. 61 (15) (2013) 5595–5604, https://doi.org/10. 1016/j.actamat.2013.06.001.
- [20] D.M. Saylor, J. Fridy, B.S. El-Dasher, K.-Y. Jung, A.D. Rollett, Statistically representative three-dimensional microstructures based on orthogonal observation sections, Metall. Mater. Trans. A 35 (7) (2004) 1969–1979, https://doi.org/10.1007/s11661-004-0146-0.
- [21] P. Hovington, P. Pinard, M. Lagacé, L. Rodrigue, R. Gauvin, M. Trudeau, Towards a more comprehensive microstructural analysis of zr-2.5nb pressure tubing using image analysis and electron backscattered diffraction (ebsd), J. Nucl. Mater. 393 (1) (2009) 162–174, https://doi.org/10.1016/j.jnucmat.2009.05.017.
- [22] A.K. Dahle, K. Nogita, J.W. Zindel, S.D. McDonald, L.M. Hogan, Eutectic nucleation and growth in hypoeutectic Al-Si alloys at different strontium levels, Metall. Mater. Trans. A 32 (4) (2001) 949–960, https://doi.org/10.1007/s11661-001-0352-y.
- [23] E. Heyn, Short reports from the metallurgical laboratory of the Royal Mechanical and Testing Institute of Charlottenburg, Metallographist 5 (1903) 37–64.
- [24] S. Torquato, B. Lu, Chord-length distribution function for two-phase random media, Phys. Rev. E 47 (4) (1993) 2950–2953, https://doi.org/10.1103/PhysRevE.47. 2950
- [25] A.P. Roberts, S. Torquato, Chord-distribution functions of three-dimensional random media: approximate first-passage times of Gaussian processes, Phys. Rev. E Stat. Phys. Plasmas Fluids Relat. Interdiscip. Topics 59 (5) (1999) 4953–4963, https://doi.org/10.1103/PhysRevE.59.4953.
- [26] ASTM Standard, E112-13, Standard Test Methods for Determining Average Grain Size, ASTM International, West Conshohocken, PA, 2013, https://doi.org/10.1520/ F0112
- [27] ASTM Standard, E1382-97(2015), Standard Test Methods for Determining Average Grain Size Using Semiautomatic and Automatic Image Analysis, ASTM International, West Conshohocken, PA, 2015, https://doi.org/10.1520/E1382-97R15
- [28] ASTM Standard, ASTM E1181-02(2015), Standard Test Methods for Characterizing Duplex Grain Sizes, ASTM International, West Conshohocken, PA, 2015, https://doi.org/10.1520/E1181-02R15.
- [29] H. Singh, A.M. Gokhale, S.I. Lieberman, S. Tamirisakandala, Image based computations of lineal path probability distributions for microstructure representation, Mater. Sci. Eng. A 474 (1–2) (2008) 104–111, https://doi.org/10.1016/j.msea. 2007.03.099.
- [30] D.M. Turner, S.R. Niezgoda, S.R. Kalidindi, Efficient computation of the angularly resolved chord length distributions and lineal path functions in large microstructure datasets, Model. Simul. Mater. Sci. Eng. 24 (7) (2016) 75002, https://doi.org/10. 1088/0965-0393/24/7/075002.
- [31] J.E. Bresenham, Algorithm for computer control of a digital plotter, IBM Syst. J. 4 (1) (1965) 25–30, https://doi.org/10.1147/sj.41.0025.
- [32] S.J. Owen, J.A. Brown, C.D. Ernst, H. Lim, K.N. Long, Hexahedral mesh generation for computational materials modeling, Procedia Eng. 203 (2017) 167–179, https://doi.org/10.1016/j.proeng.2017.09.803.
- [33] E. Popova, T.M. Rodgers, X. Gong, A. Cecen, J.D. Madison, S.R. Kalidindi, Process-structure linkages using a data science approach: application to simulated additive manufacturing data, Integr. Mater. Manuf. Innov. 6 (1) (2017) 54–68, https://doi.org/10.1007/s40192-017-0088-1.
- [34] M.I. Latypov, S.R. Kalidindi, Data-driven reduced order models for effective yield strength and partitioning of strain in multiphase materials, J. Comput. Phys. 346 (2017) 242–261, https://doi.org/10.1016/j.jcp.2017.06.013.
- [35] M.I. Latypov, L.S. Toth, S.R. Kalidindi, Microstructure-sensitive models for non-linear composites, Comput. Methods Appl. Mech. Eng. (2018) (Under Review), arXiv preprint arXiv:1807.11313. https://arxiv.org/abs/1809.07484
- arXiv preprint arXiv:1807.11313, https://arxiv.org/abs/1809.07484.
  [36] A. Khosravani, A. Cecen, S.R. Kalidindi, Development of high throughput assays for establishing process-structure-property linkages in multiphase polycrystalline metals: application to dual-phase steels, Acta Mater. 123 (2017) 55–69, https://doi.org/10.1016/j.actamat.2016.10.033.
- [37] C. Mießen, N. Velinov, G. Gottstein, L.A. Barrales-Mora, A highly efficient 3D level-set grain growth algorithm tailored for ccNUMA architecture, Model. Simul. Mater. Sci. Eng. 25 (8) (2017), https://doi.org/10.1088/1361-651X/aa8676.
- [38] S.R. Ghorpade, B.V. Limaye, A Course in Calculus and Real Analysis, The Australian Mathematical Society, 2008, p. 211.
- [39] P. Bourke, Intersection Point of Two Line Segments in 2 Dimensions, http://paulbourke.net/geometry/pointlineplane/, (1989) (accessed Sep. 21, 2018).
- [40] D. Rowenhorst, A.D. Rollett, G.S. Rohrer, M. Groeber, M. Jackson, P.J. Konijnenberg, M. De Graef, Consistent representations of and conversions between 3D rotations, Model. Simul. Mater. Sci. Eng. 23 (8) (2015), https://doi.org/10.1088/0965-0393/23/8/083501.
- [41] EDAX, OIM Analysis: User Manual, v.8, (2016).
- [42] R. Bro, A.K. Smilde, Principal component analysis, Anal. Methods 6 (9) (2014) 2812–2831, https://doi.org/10.1039/C3AY41907J.
- [43] K. Pearson, LIII. On lines and planes of closest fit to systems of points in space, Philos. Mag. Ser. 6 2 (11) (1901) 559–572, https://doi.org/10.1080/ 14786440109462720.
- [44] S.R. Niezgoda, A.K. Kanjarla, S.R. Kalidindi, Novel microstructure quantification framework for databasing, visualization, and analysis of microstructure data, Integr. Mater. Manuf. Innov. 2 (1) (2013) 1–27, https://doi.org/10.1186/2193-9772-2-3.

- [45] S.R. Niezgoda, Y.C. Yabansu, S.R. Kalidindi, Understanding and visualizing microstructure and microstructure variance as a stochastic process, Acta Mater. 59 (16) (2011) 6387–6400, https://doi.org/10.1016/j.actamat.2011.06.051.
- [46] M.A. Groeber, M.A. Jackson, DREAM.3D: a digital representation environment for the analysis of microstructure in 3D, Integr. Mater. Manuf. Innov. 3 (2014) 1–17, https://doi.org/10.1186/2193-9772-3-5.
- [47] M. Groeber, S. Ghosh, M.D. Uchic, D.M. Dimiduk, A framework for automated analysis and simulation of 3D polycrystalline microstructures. Part 2: synthetic structure generation, Acta Mater. 56 (6) (2008) 1274–1287, https://doi.org/10. 1016/j.actamat.2007.11.040.
- [48] F. Bachmann, R. Hielscher, H. Schaeben, Texture analysis with MTEX free and open source software toolbox, Solid State Phenom. 160 (2010) 63–68, https://doi. org/10.4028/www.scientific.net/SSP.160.63.
- [49] F. Bachmann, R. Hielscher, H. Schaeben, Grain detection from 2d and 3d EBSD data-specification of the MTEX algorithm, Ultramicroscopy 111 (12) (2011) 1720–1733, https://doi.org/10.1016/j.ultramic.2011.08.002.
- [50] M. Diehl, M. Groeber, C. Haase, D.A. Molodov, F. Roters, D. Raabe, Identifying structure-property relationships through DREAM.3D representative volume elements and DAMASK crystal plasticity simulations: an integrated computational materials engineering approach, JOM 69 (5) (2017) 848–855, https://doi.org/10. 1007/s11837-017-2303-0.
- [51] R.C. Reed, The Superalloys: Fundamentals and Applications, Cambridge University Press, 2006, https://doi.org/10.1017/CBO9780511541285.
- [52] V. Randle, Grain boundary engineering: an overview after 25 years, Mater. Sci. Technol. 26 (3) (2010) 253–261, https://doi.org/10.1179/ 026708309X12601952777747.
- [53] T. Ezaz, M.D. Sangid, H. Sehitoglu, Energy barriers associated with slip-twin interactions, Philos. Mag. 91 (10) (2011) 1464–1488, https://doi.org/10.1080/14786435.2010.541166.
- [54] S. Xu, L. Xiong, Y. Chen, D.L. McDowell, Sequential slip transfer of mixed-character dislocations across Σ3 coherent twin boundary in FCC metals: a concurrent atomistic-continuum study, npj Comput. Mater. 2 (December 2015), https://doi.org/ 10.1038/npjcompumats.2015.16.
- [55] J.C. Stinville, E. Martin, M. Karadge, S. Ismonov, M. Soare, T. Hanlon, S. Sundaram, M.P. Echlin, P.G. Callahan, W.C. Lenthe, V. Miller, J. Miao, A.E. Wessman, R. Finlay, A. Loghin, J. Marte, T.M. Pollock, Fatigue deformation in a polycrystal-line nickel base superalloy at intermediate and high temperature: competing failure modes, Acta Mater. 152 (2018) 16–33, https://doi.org/10.1016/j.actamat.2018.03.
- [56] R.C. Boettner, A.J. McEvily Jr., C.Y. Liu, On the formation of fatigue cracks at twin boundaries, Philos. Mag. 10 (103) (1964) 95–106, https://doi.org/10.1080/ 14786436408224210.
- [57] J.C. Stinville, W.C. Lenthe, J. Miao, T.M. Pollock, A combined grain scale elastic-plastic criterion for identification of fatigue crack initiation sites in a twin containing polycrystalline nickel-base superalloy, Acta Mater. 103 (2015) 461–473, https://doi.org/10.1016/j.actamat.2015.09.050.
- [58] C.A. Stein, S. Lee, A.D. Rollett, An analysis of fatigue crack initiation using 2D orientation mapping and full-field simulation of elastic stress response, superalloys, Superalloys, 2012: Proceedings of the 12th International Symposium on Superalloys, Wiley, 201210.1002/9781118516430.ch48.
- [59] A. Heinz, P. Neumann, Crack initiation during high cycle fatigue of an austenitic steel, Acta Metall. Mater. 38 (10) (1990) 1933–1940, https://doi.org/10.1016/ 0956-7151(90)90305-7
- [60] J.C. Stinville, W.C. Lenthe, M.P. Echlin, P.G. Callahan, D. Texier, T.M. Pollock, Microstructural statistics for fatigue crack initiation in polycrystalline nickel-base superalloys, Int. J. Fract. (2017) 1–20, https://doi.org/10.1007/s10704-017-0241-7
- [61] M.I. Latypov, J.-C. Stinville, J.R. Mayeur, T.M. Pollock, I.J. Beyerlein, Micromechanical study of elastic strain localization in René 88DT with annealing twin boundaries (In Preparation).
- [62] D.D. Krueger, R.D. Kissinger, R.G. Menzies, Developement and introduction of a damage tolerant high temperature nickel-base disk alloy, Rene 88DT, Superalloys 1992, vol. 7, The Minerals, Metals & Materials Society, 1992.
- [63] W.C. Lenthe, J.-C. Stinville, M.P. Echlin, T.M. Pollock, Statistical Assessment of Fatigue-Initiating Microstructural Features in a Polycrystalline Disk Alloy, Superalloys 2016: Proceedings of the 13th International Symposium, Wiley, 2016, , https://doi.org/10.1002/9781119075646.ch61.
- [64] R.D. Doherty, D.A. Hughes, F.J. Humphreys, J.J. Jonas, D. Juul Jensen, M.E. Kassner, W.E. King, T.R. McNelley, H.J. McQueen, A.D. Rollett, Current issues in recrystallization: a review, Mater. Sci. Eng. A 238 (2) (1997) 219–274, https://doi.org/10.1016/S0921-5093(97)00424-3.
- [65] M. Kühbach, On the significance of microstructure property topography and capillary contributions for nucleating abnormal grain growth and recrystallization, Acta Mater. (2018) (Under Review).
- [66] N. Leuning, S. Steentjes, A. Stöcker, R. Kawalla, X. Wei, J. Dierdorf, G. Hirt, S. Roggenbuck, S. Korte-Kerzel, H.A. Weiss, W. Volk, K. Hameyer, Impact of the interaction of material production and mechanical processing on the magnetic properties of non-oriented electrical steels, AIP Adv. 8 (2018), https://doi.org/10. 1063/1.4994143.
- [67] G. Ibe, K. Lücke, Growth selection during recrystallization of single crystals, Recrystallization, Grain Growth and Textures, 1966, p. 434.
- [68] A. Derossi, T. De Pilli, C. Severini, Statistical description of fat and meat phases of sausages by the use of lineal-path distribution function, Food Biophys. 7 (3) (2012) 258–263, https://doi.org/10.1007/s11483-012-9264-1.